Nano Energy 103 (2022) 107816

Contents lists available at ScienceDirect

Nano Energy

journal homepage: www.elsevier.com/locate/nanoen

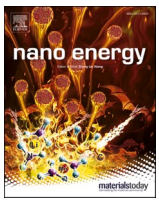

General analysis and optimization of a two-stage power management circuit for electrostatic/triboelectric nanogenerators

Hemin Zhang [a,b], Dimitri Galayko [c,1], Philippe Basset [a,*,1]

[a] Univ Gustave Eiffel, CNRS, ESYCOM, F-77454 Marne-la-Vallée, France
[b] Ministry of Education Key Laboratory of Micro and Nano Systems for Aerospace, Northwestern Polytechnical University, Xi'an 710072, PR China
[c] Sorbonne Université, CNRS, LIP6, Paris, France

ARTICLE INFO

Keywords:
Triboelectric nanogenerator
Full-wave rectifier
Half-wave rectifier
DC-DC buck converter
Hysteresis automatic electrostatic switch

ABSTRACT

Triboelectric nanogenerators (TENGs) generate high AC voltages that are often rectified using stable charge pumps. This paper provides for the first time a comprehensive general theory that determines the optimal electrical bias conditions for this class of rectifiers. In this work, the proposed generic formulas have been applied to full-wave and half-wave diode bridges. Key figures have been demonstrated like for instance the optimal bias voltage or the maximum converted energy. It is confirmed that half-wave rectifiers always have a higher saturated voltage, as well as higher maximum energy per cycle, but at the cost of longer start-up time. On the contrary, full-wave rectifiers perform better only when the output voltage is much lower than the internal triboelectric voltage of the TENG. These rectifiers followed by a buck DC-DC converter have also been studied in details, often required to provide a low output voltage. We showed that the optimal buck' switch activation is between .5 and .7 of the charge-pump saturation voltage, depending on the hysteresis of the switch, and that the charging time of the output capacitor is at least twice as fast with a half-wave rectifier than with a full-wave rectifier. The theoretical results were confirmed by simulations and experiments using a plasma switch.

1. Introduction

Triboelectric nanogenerators (TENGs) [1] are particular electrostatic kinetic energy harvesters (e-KEH) [2] that couple the principles of contact electrification and electrostatic induction through the variation of a transducer capacitance [3]. Basically, the physical contact of two materials with different abilities of attracting electrons traps electrons inside at least one tribo-electret layer, which is an insulator. Opposite charges are induced on the surfaces of the two neighboring electrodes, and a current will occur between them to rebalance the electrostatic field when their capacitance changes due to the application of external mechanical forces.

TENGs typically generate high-voltage open-circuit pulses, with peak voltages ranging from tens of volts to several kV. Efficient storage of such high pulsed AC voltage to power low DC voltage electronic devices remains a practical problem and a voltage AC-to-DC rectifier is needed. The power management circuit (PMC) can be made of passive charge pumps implemented with electrical diodes or with mechanical switches [4,5]. The most common rectifiers are Full-wave (FW) and half-wave (HW) diode bridges that can be considered as stable charge pumps (SCP) because of the saturation of their output voltage, and the conditioning circuits from the Bennet doubler family are unstable charge pumps (UCP). In addition, it has been proposed to use PMC based on the synchronous technics such as SECE (for Synchronous Electrical Charge Extraction) or SSHI (for Synchronous Switching Harvesting on Inductor) [6]. These technics have been initially proposed for piezoelectric generators and further applied to TENGs [7–9]. It consists in using an inductive DC-DC convertor activated synchronously with the motion of the mobile electrode for externally controlling the TENG's current.

However, these types of direct energy transfer are inefficient due to the large difference between the capacitance of the TENG and the output (storage) capacitance of the rectifier [10,11]: indeed, a large output capacitor is usually required to store a sufficient amount of harvested energy, especially when a low DC voltage is required. Significant improvement of several orders of magnitude can be obtained with a two-stage PMC [10,11]: an intermediate value buffer capacitor is first quickly charged to an optimized high voltage corresponding to the maximum energy extraction rate, then the energy is steadily transferred

* Corresponding author.
E-mail address: philippe.basset@esiee.fr (P. Basset).
[1] The two authors have the same contribution to this study

https://doi.org/10.1016/j.nanoen.2022.107816
Received 7 July 2022; Received in revised form 12 September 2022; Accepted 15 September 2022
Available online 17 September 2022

to the larger-capacity and low-voltage reservoir with this maximum power. This requires the use of a dedicated switch, so motion-triggered switches [9,12,13], electronic switches [7,8], electrostatic vibration switch [14,15] or micro-plasma switches [11] have been developed.

The voltage of the buffer must be maximized, as the energy transduction evolves with the square of this voltage [2]. For this reason, UCP such as the Bennet doubler might be appropriate [16–18], as they eliminate the limiting nature of the voltage saturation of HW/FW rectifiers. However, UCP may not always be appropriate because it requests a minimum capacitance variation for every cycle, which is typically 2 for the conventional configuration [17,18]. Moreover, if the converted energy needs to be available in a very short time, HW and FW rectifiers may be more efficient than UCP [19,20].

In a previous work, the operation principles of FW and HW rectifiers in a 1-stage PMC, using time-domain evaluations or charge-voltage (QV) cycles [20] have been explored. In this paper, the focus is both theoretically and experimentally on the optimized operating voltages of these rectifiers while employing a hysteresis switch in a 2-stage PMC, which has not been studied before. In the following section, the basic operating principles are theoretically derived for any type of stable charge pumps for the first time, and we applied the obtained formulas to FW/HW rectifiers. Then, we analyzed the power transfer efficiencies using different types of switches in the 2-stage PMC, and studied the optimized voltages in different configurations. Finally, the proposed theory is demonstrated by experiments with a TENG.

2. Theoretical analysis of one stage conditioning circuits

2.1. The transducer electrical model

The structure and its equivalent capacitive model of the electrostatic transducer used in this study are shown in Fig. 1. The dielectric layer attached to the lower electrode is an electret of dielectric constant $\mathcal{E}$. It can be charged by different techniques such as corona discharge, soft x-ray or triboelectric contacts [21], so it is called the tribo-electret (TE) layer. It is assumed to have a localized Q_{TE} charge on an (infinitely) thin layer on the surface that remains constant. In the case of TENGs, the latter assumption is true after a few cycles of motion as long as the contact force does not increase. The upper electrode is free to move along the vertical axis, d_{var} varying from 0 to some maximum value allowed by the device geometry. The top and bottom electrodes have the charges Q_{var} and Q_{die} respectively. The electrical equation is derived using the neutrality assumption generally accepted in circuit theory. This assumption states that any electrical component is electrically neutral. That implies the following equality:

$$Q_{var} + Q_{TE} + Q_{die} = 0 \tag{1}$$

Q_{TE} is equal to the surface charge density of the dielectric multiplied by its contact area S, with charge density $\sigma = Q_{TE}/S$. Considering Q_{TE} as a known constant quantity (it can be derived by indirect measurements [22,23]), using the Gauss theorem the voltage across the TENG's terminals can be expressed as

$$V_{TENG} = Q_{var}\left(\frac{d_{die}}{S\varepsilon_0\varepsilon_{die}} + \frac{d_{var}}{S\varepsilon_0}\right) + Q_{TE}\frac{d_{die}}{S\varepsilon_0\varepsilon_{die}} \tag{2}$$

Note that by convention, the voltage V_{TENG} is defined as the voltage difference between the top and bottom electrodes, with the top electrode considered conventionally positive. In this work, the positive TENG current i_{TENG} is defined by convention as flowing into the positive (top) electrode, and thus

$$i_{TENG} = \frac{dQ_{var}}{dt} = -\frac{dQ_{die}}{dt} \tag{3}$$

Setting

$$C_{die} = \varepsilon_0\varepsilon_{die}\frac{S}{d_{die}}, \quad C_{var} = \varepsilon_0\frac{S}{d_{var}} \tag{4}$$

The capacitance that can be physically measured across the TENG's terminals called C_{TENG} is defined as

$$C_{TENG} = \frac{C_{var}C_{die}}{C_{var} + C_{die}} = \varepsilon_0\frac{S}{d_{var} + d_{die}/\varepsilon_{die}} \tag{5}$$

where C_{die} is the capacitance of the tribo-electret layer having the relative permittivity $\mathcal{E}_{die}$, and is equal to the maximum capacitance value of the TENG. C_{var} represents the variable part of the TENG's capacitor due to the displacement of the moving electrode.

The quantity $V_{TE} = Q_{TE}\frac{d_{die}}{S\varepsilon_0\varepsilon_{die}}$ is called "built-in voltage of the TENG":

$$V_{TE} = \frac{Q_{TE}}{C_{die}} = \frac{Q_{TE}}{C_{T\_max}} = \frac{\sigma d_{die}}{\varepsilon_{die}\varepsilon_0} \tag{6}$$

V_{TE} is the internal bias voltage created by the tribo-electret layer. It is a constant value that corresponds to the average surface voltage of the tribo-electret layer, which can be measured directly using an electrometer (but its value will be quite inaccurate due to its non-uniformity over the whole layer surface) or indirectly measured using dedicated methods [22,23], even if the charged surface is not accessible.

Finally, by injecting (5) and (6) into (2), a charged TENG can be modelled as a variable capacitor and a DC voltage source connected in series (Fig. 2a):

$$V_{TENG} = V_{TE} + \frac{Q_{var}}{C_{TENG}} = V_{TE} + V_{var} \tag{7}$$

Q_{var} is the charge stored by the top electrode. It cannot be measured directly, however, its derivative is equal to the electric current flowing through the TENG electrodes, as mentioned earlier. The quantity $\frac{Q_{var}}{C_{TENG}} = V_{var}$ is the voltage across an equivalent variable capacitance. This quantity is an internal variable of the model. It does not correspond to any measurable voltage, and it is related with V_{TENG} (which is directly measurable) by (7). It should be noted that the built-in charge of the dielectric layer defines the polarity of the TENG, and that swapping its terminals leads to a different electrical equation. Indeed, swapping the terminals is equivalent to multiplying the left hand-side of (7) by − 1 (see Fig. 2b).

$$V_{TENG} = -V_{TE} - \frac{Q_{var}}{C_{TENG}} \tag{8}$$

Moreover, since Q_{var} is an internal parameter of the model and is not directly measurable, we can now define $Q_{var} \rightarrow -Q_{var}$, which corresponds to interchanging the order of the terminals of C_{var}, and doesn't affect the model (see Fig. 2c). The new equation of the device becomes

$$V_{TENG} = -V_{TE} + \frac{Q_{var}}{C_{TENG}} \tag{9}$$

Since the order of the C_{TENG} and V_{TE} is not important, swapping the terminals is equivalent to changing the sign of the charge Q_{TE} (compare

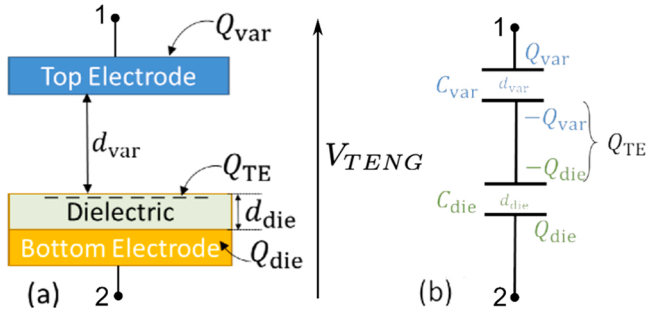

Fig. 1. Structure of an electrostatic kinetic energy harvester corresponding to a metal/dielectric TENG. Structural diagram for gap-closing motion (a) and capacitive model (b).

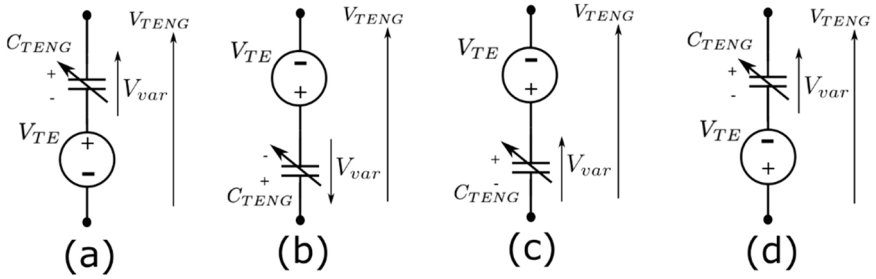

Fig. 2. Electrical equivalent models of the TENG. Model corresponding to Eq. (7) (a), the same model with swapped terminal corresponding to the Eq. (8) (b), the equivalent model of the latter corresponding to the Eq. (9) (c,d).

Eq. (7) and Eq. (9), Figs. 2a and 2d). It can be seen that Eqs. (7), (8) and (9) are different, and therefore the behaviour of the circuits is sensitive to the polarity used to connect the TENG and to the sign of the built-in charge Q_{TE}. This point must be taken into account when analysing non-symmetrical circuits such as half-wave rectifier and Bennet's doubler (see sect. II.E).

The first model derived specifically for a TENG was presented by Niu et al. [24,25]. Although expressed differently, the model presented here is strictly equivalent. The model used in this paper expresses the voltage V_{TENG} by the charge of the top electrode Q_{var} as is traditionally done for electret kinetic energy harvesters, whereas Niu's model expresses the voltage V_{TENG} by the charge of the bottom electrode Q_{die}. In that case, V_{TENG} is given by

$$V_{TENG} = V_{TE} + \frac{-Q_{TE} - Q_{die}}{C_{TENG}} = \frac{Q_{TE}}{C_{TENG}} - Q_{TE}\left(\frac{1}{C_{var}} + \frac{1}{C_{die}}\right) - \frac{Q_{die}}{C_{TENG}}$$
$$= -\frac{Q_{TE}}{C_{var}} - \frac{Q_{die}}{C_{TENG}} \tag{10}$$

Expressing Q_{TE} in terms of the surface charge density of the TE layer σ leads to

$$V_{TENG} = -\frac{\sigma x(t)}{\varepsilon_0} - \frac{Q_{die}}{C_{TENG}} \tag{11}$$

Again, since Q_{die} is an internal quantity, it can be replaced it by $-Q_{die}$, which means that the positive device current is redefined as entering the positive (upper) terminal (see Eq. (3)). We get

$$V_{TENG} = -\frac{\sigma x(t)}{\varepsilon_0} + \frac{Q_{die}}{C_{TENG}} \tag{12}$$

This model corresponds to an equivalent circuit comprising a variable capacitor C_{TENG} and a variable voltage source, whose variations are mathematically linked to that of C_{TENG}.

The two models are strictly equivalent in the sense that Q_{die} and Q_{var}, being different and not directly measurable, have the same time derivative and therefore define the same electrical current i_{TENG}. However, the model in Fig. 2 has a distinct advantage: it includes a DC voltage source instead of a variable voltage source, which makes the analysis and modeling much simpler. For instance, energy conversion is only performed by the variable capacitor, since the DC voltage source in series with a capacitor doesn't generate energy in average when operating in the periodic mode. This allows one to re-use the analysis tools developed for the kinetic energy harvesters using variable capacitors and electret-biased transducers. This model will be used in our work.

In this article, the analysis is done under the following convention: after shorting the TENG at C_{TENG}=C_{T_max} (initialization of Q_{var}), in open circuit configuration, the voltage V_{TENG} increases and becomes positive when C_{TENG} decreases. Such a behaviour corresponds to a negative charge Q_{TE} and hence to the model shown in Fig. 2c,d.

The value of V_{TE} has a direct effect on the energy conversion performance of the TENG: indeed, all key performance figures are proportional to V_{TE}^2, so maximizing V_{TE} is sought. Since V_{TE} is proportional to the surface charge density σ, researchers have developed various methods to increase σ [26,27]. The influence of the thickness and permittivity of the tribo-electret layer has also been discussed [28].

In this paper, it is assumed a motion of the mobile electrode such that the capacitance varies periodically with period T, with only a maximum and a minimum in one a period, and with a fixed max/min ratio $\eta = \frac{C_{T\_max}}{C_{T\_min}}$, where C_{T_max} and C_{T_min} represent the maximum and minimum value of C_{TENG} respectively.

2.2. Generic dynamics of capacitive charge-pumps using TENGs

TENGs can be used in a range of capacitive charge pumps that generate a DC output voltage: half-wave and full wave rectifiers, voltage multipliers, unstable charge pumps [16–18], etc. The operation of these charge pumps results in an increase of the voltage on C_{rect}, output capacitor of the charge-pump, throughout the variation cycles of C_{TENG}. This evolution is governed by the following generic law:

$$V_{i+1} = \alpha V_i + \beta \tag{13}$$

where α and β are coefficients depending on the TENG parameters and the charge pump architecture, V_i being the output voltage at the i^{th} cycle. A cycle of a capacitance variation starts at the moment when C_{TENG}=C_{T_max}. This voltage evolution corresponds to an energy accumulation on the capacitor C_{rect}, which can be calculated as follows:

$$E_i = \frac{C_{rect}}{2} V_i^2 \tag{14}$$

The energy produced during cycle i is given by

$$\Delta E_i = \frac{C_{rect}}{2}\left[(\alpha V_i + \beta)^2 - V_i^2\right] = \frac{C_{rect}}{2}\left[(\alpha^2 - 1)V_i^2 + 2\alpha\beta V_i + \beta^2\right] \tag{15}$$

In most practical cases, α is close to unity.

2.3. Key quantities for stable charge-pumps using TENGs

For analysis, it is useful to introduce an additional parameter $\epsilon = 1 - \alpha$ so that $\alpha = 1 - \epsilon$. Some figures are interesting for the practical use of charge pumps in the energy converters.

- **The saturation voltage** (as $i \to \infty$): The charge pump saturates if and only if $\alpha < 1$. In this case the saturation voltage V_{sat} is found from (13) knowing that

$$V_{\infty+1} = \alpha V_\infty + \beta = \quad V_\infty = V_{sat} \Longrightarrow V_{sat} = \frac{\beta}{1-\alpha} = \frac{\beta}{\epsilon} \tag{16}$$

- **The maximum energy converted during one cycle and the corresponding output voltage.** If $\alpha < 1$, Eq. (15) has a maximum over V_i which is given by

$$V_{opt} = \frac{\left(\frac{1}{\epsilon} - 1\right)\beta}{2 - \epsilon}, \qquad \Delta E_{max} = \frac{C_{rect}}{2}\frac{\beta^2}{\epsilon(2-\epsilon)} \tag{17}$$

If $\epsilon << 1$, these formulas simplify as follow

$$V_{opt} \approx \frac{\beta}{2\epsilon} \quad , \quad \Delta E_{max} = \frac{C_{rect}}{2}\frac{\beta^2}{2\epsilon} \tag{18}$$

- **The energy generated at the beginning**, when the output voltage is close to zero. According to (15), this energy is given by

$$\Delta E_0 = \frac{C_{rect}}{2}\beta^2 \tag{19}$$

- **The transient time**. This is the number of cycles required to reach 95% of the saturation voltage, when started from zero. To find it, V_i should be expressed explicitly. Solving the recurrence Eq. (13) gives

$$V_i = \left(V_0 - \frac{\beta}{\epsilon}\right)(1-\epsilon)^i + \frac{\beta}{\epsilon} \tag{20}$$

where V_0 is the output voltage (the pre-charge of C_{rect}) at the beginning of the cycle $i = 1$.

Note that if ϵ is positive (this is always the case for the saturated charge pumps) and close to zero (usually the case in practice), the equation can be rewritten as

$$V_i \approx \left(V_0 - \frac{\beta}{\epsilon}\right)\exp(-i\epsilon) + \frac{\beta}{\epsilon} \tag{21}$$

The number of cycles required to reach 95% of saturation i_{sat} can be obtained from this equation by requiring

$$V_i = 0.95\frac{\beta}{\epsilon}, V_0 = 0 \tag{22}$$

Leading to

$$i_{sat} = -\frac{1}{\epsilon}\ln 0.05 \approx \frac{3}{\epsilon} \tag{23}$$

- **Average energy per cycle after *i* first cycles**. In some cases, it is interesting to know the average energy per cycle (average power) when the charge pump starts from zero output voltage and run i cycles. The corresponding formula is obtained from (21) by setting $V_0 = 0$:

$$E_{avgi} = \frac{1}{i}\frac{C_{rect}V_i^2}{2} = \frac{1}{i}\frac{C_{rect}}{2}\left(\frac{\beta}{\epsilon}[1-(1-\epsilon)^i]\right)^2 \tag{24}$$

If $\epsilon \ll 1$, it can be simplified to

$$E_{avgi} = \frac{1}{i}\frac{C_{rect}V_i^2}{2} = \frac{1}{i}\frac{C_{rect}}{2}\left(\frac{\beta}{\epsilon}[1-\exp(-i\epsilon)]\right)^2 \tag{25}$$

In the next two sections the analysis of the full-wave and half-wave rectifiers will be presented, with the aim of finding the parameters α and β. Then, the generic formulas just presented will be used to compare the circuits.

2.4. Dynamic equations for full-wave rectifiers

The analysis of the FW rectifier starts from the following initial state:

$$\left\{\begin{array}{c} V_s = V_{s\bar{i}} \\ V_{var} = V_{TE} - V_{s\bar{i}} \\ C_{TENG} = C_{T\_max} \end{array}\right\} \tag{26}$$

where V_s is the output voltage of the rectifier (the voltage the capacitor C_{rect}, see Fig. 3). The subscript i denotes the cycle number. An upper bar on i denotes the voltage value when C_{TENG}=C_{T_max} ($V_{s\bar{i}}$), and the lower bar denotes the voltage when C_{TENG}=C_{T_min} ($V_{s\underline{i}}$). An ideal diode model has been used: the forward voltage and reverse leakage current of the diodes are zero. The minus sign in front of $V_{s\bar{i}}$ in the second equation of (26) is due to the fact that the previous cycle (i-1) ended with diodes D4 and D2 conducting.

The operation of the full-wave rectifier (Fig. 3a) and the energy conversion process can be characterized by the QV cycle presented in Fig. 3b. The circuit state starts at the point A and follows the clockwise direction.

2.4.1. Evolution from C_{T_max} to C_{T_min}

Segment A→B: As C_{TENG} decreases, its voltage increases and as far as $V_{TENG} = V_{var} - V_{TE} < V_{s\bar{i}}$, the diodes are OFF, Q_{var} is constant and is equal to

$$Q_1 = C_{T\_max}(V_{TE} - V_{s\bar{i}}) \tag{27}$$

The point B is characterized by the value of C_{TENG} equal to $\frac{Q_1}{V_{TE}+V_{s\bar{i}}}$. Starting from this point, the diodes D1 and D3 are ON, and the capacitor C_{rect} is in series with the TENG, so that "+ " terminal of C_{rect} is connected to "+ " terminal of C_{TENG}. During the segment BC, the sum of charges on these two capacitor's electrodes is constant and is equal to Q^* . Calculated from point B, it gives

$$Q^* = Q_1 + C_{rect}V_{s\bar{i}} = C_{T\_max}(V_{TE} - V_{s\bar{i}}) + C_{rect}V_{s\bar{i}} \tag{28}$$

At point C, the same charge is redistributed differently over C_{rect} and C_{TENG}, then

$$Q^* = C_{T\_min}(V_{TE} + V_{s\underline{i}}) + C_{rect}V_{s\underline{i}} \tag{29}$$

Equating these two expressions gives

$$V_{s\underline{i}} = \frac{C_{T\_max}(V_{TE} - V_{s\bar{i}}) + C_{rect}V_{s\bar{i}} - C_{T\_min}V_{TE}}{C_{T\_min} + C_{rect}} \tag{30}$$

2.4.2. Evolution from C_{T_min} to C_{T_max}

The same analysis allows one to calculate the voltage V_s at the point

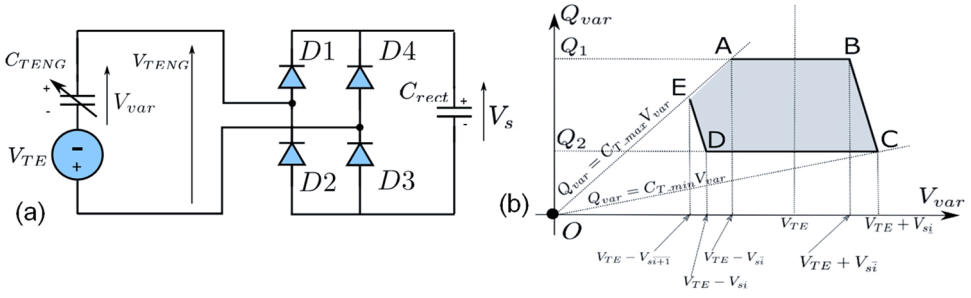

Fig. 3. (a) Schematic of a full-wave rectifier, (b) QV cycle of the variable capacitor C_{TENG} in a full-wave rectifier, where Q_{var} and V_{var} represent the charge on and the voltage across C_{TENG} respectively.

E. As C_{TENG} starts to increase from point C, its voltage decreases and all diodes are off. The charge of C_{TENG} is constant as far as $V_{var} > V_{TE} - V_{s\bar{i}}$. Then from point C to point D, it is equal to

$$Q_2 = C_{T\_min}(V_{TE} + V_{s\bar{i}}) \tag{31}$$

The point D is characterized by the value of the variable capacitance given by $\frac{Q_2}{V_{TE}-V_{s\bar{i}}}$. Starting from the point D, diodes D2 and D4 are ON and C_{rect} is connected to the TENG, so that the "-" terminal of C_{rect} is connected to "+ " terminal of C_{var}. During the segment DE, the sum of charges on these electrodes is constant. At point D, it is expressed as

$$Q^{**} = Q_2 - C_{rect}V_{s\bar{i}} = C_{T\_min}(V_{TE} + V_{s\bar{i}}) - C_{rect}V_{s\bar{i}} \tag{32}$$

Note that the charge on the electrode "-" of C_{rect} is taken with the minus sign.

At point E, the same charge can be expressed:

$$Q^{**} = C_{T\_max}(V_{TE} - V_{s\overline{i+1}}) - C_{rect}V_{s\overline{i+1}} \tag{33}$$

Equating these two expressions leads to

$$V_{s\ \overline{i+1}} = \frac{C_{T\_min}\left(V_{TE} + V_{s\bar{i}}\right) - C_{rect}V_{s\bar{i}} - C_{T\_max}V_{TE}}{-C_{T\_max} - C_{rect}} \tag{34}$$

Combining (30) and (34):

$$V_{s\overline{i+1}} = V_{s\bar{i}}\frac{C_{rect} - C_{T\_min}}{C_{T\_max} + C_{rect}}\frac{C_{rect} - C_{T\_max}}{C_{T\_min} + C_{rect}} + V_{TE}\frac{2C_{rect}(C_{T\_max} - C_{T\_min})}{(C_{T\_max} + C_{rect})(C_{T\_min} + C_{rect})} \tag{35}$$

Setting $\zeta = \frac{C_{rect}}{C_{Tmin}}$. and $\eta = \frac{C_{Tmax}}{C_{Tmin}}$, we get

$$V_{s\overline{i+1}} = V_{s\bar{i}}\frac{\zeta - 1}{\zeta + \eta}\bullet\frac{\zeta - \eta}{\zeta + 1} + V_{TE}\frac{2\zeta(\eta - 1)}{(\zeta + \eta)(\zeta + 1)} \tag{36}$$

This recurrence equation fully characterizes the dynamics of the voltage V_s, with α et β in (13) given by

$$\alpha = \frac{\zeta - 1}{\zeta + 1}\bullet\frac{\zeta - \eta}{\zeta + \eta} \tag{37}$$

$$\beta = V_{TE}\frac{2\zeta(\eta - 1)}{(\zeta + \eta)(\zeta + 1)} \tag{38}$$

2.5. Dynamic equations for half-wave rectifiers

The half wave rectifier (Fig. 4a) operates similarly with the full wave rectifier, except that the C_{rect} capacitor is only charged during the forward ($C_{max} \rightarrow C_{min}$) phase. The corresponding QV cycle is presented in Fig. 4b. Again, the analysis of the HW rectifier starts from the following initial state:

$$\left\{\begin{array}{c} V_s = V_{s\bar{i}} \\ V_{var} = V_{TE} \\ C_{TENG} = C_{T\_max} \end{array}\right\} \tag{39}$$

2.5.1. Evolution from C_{T_max} to C_{T_min}

During the phase AB, the charge is constant and is equal to

$$Q_1 = C_{T\_max}V_{TE} \tag{40}$$

As C_{TENG} decreases, the voltage V_{var} increases till $V_{var} > V_{TE} + V_{s\bar{i}}$. At point B this becomes an equality, the diode D1 becomes ON and the capacitor C_{rect} is in series with the TENG, so that "+ " terminal of C_{rect} is connected to the "+ " terminal of C_{var}. The total charge on the electrodes "+ " of both capacitors is constant during this segment. At point B it reads

$$Q^* = Q_1 + C_{rect}V_{s\bar{i}} = C_{T\_max}V_{TE} + C_{rect}V_{s\bar{i}} \tag{41}$$

At point C the same charge, redistributed differently over C_{rect} and C_{var} is:

$$Q^* = C_{T\_min}(V_{TE} + V_{s\underline{i}}) + C_{rect}V_{s\underline{i}} \tag{42}$$

Equating the last two expressions gives

$$V_{s\underline{i}} = \frac{C_{T\_max}V_{TE} + C_{rect}V_{s\bar{i}} - C_{T\_min}V_{TE}}{C_{T\_min} + C_{rect}} \tag{43}$$

2.5.2. Evolution from C_{T_min} to C_{T_max}

Since during the phase CD and DE the diode D1 is off, the voltage V_s doesn't change till the end of the cycle, consequently

$$V_{s\overline{i+1}} = V_{s\underline{i}} = V_{s\bar{i}}\frac{C_{rect}}{C_{T\_min} + C_{rect}} + V_{TE}\frac{C_{T\_max} - C_{T\_min}}{C_{T\_min} + C_{rect}} = V_{s\bar{i}}\frac{\zeta}{\zeta + 1} + V_{TE}\frac{\eta - 1}{\zeta + 1} \tag{44}$$

This recurrence equation fully characterizes the dynamics of the voltage V_s, with α et β in (13) given by

$$\alpha = \frac{\zeta}{\zeta + 1} \tag{45}$$

$$\beta = V_{TE}\frac{\eta - 1}{\zeta + 1} \tag{46}$$

2.6. Comparative analysis of half wave (HW) and full wave (FW) rectifiers

2.6.1. Key quantities of FW and HW rectifiers

Now, the generic formulas derived in section IIB can be applied to the full wave and half wave rectifiers for comparing the key performances of the two circuits.

The following hypotheses are made for the comparative analysis:

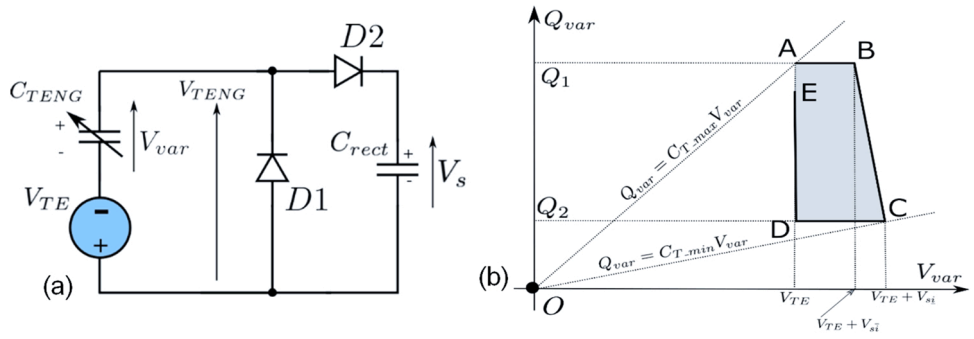

Fig. 4. (a) Schematic of a half-wave rectifier, (b) QV cycle for the variable capacitor C_{TENG} in a half-wave rectifier, where Q_{var} and V_{var} represent the charge on and the voltage across C_{TENG}, respectively.

- C_{rect} is such as $C_{rect} > > C_{Tmax}$, as a consequence $\zeta \gg 1$ and $\zeta \gg \eta$. For both rectifiers, this means $\epsilon \ll 1$. This hypothesis is generally verified in applications, given the typical capacitance values of TENGs
- Zero initial voltage of C_{rect} is considered, i.e. $V_0 = 0$ in the formulas (20) and (21).

Given these, the formulas for the parameters of the full wave and half wave rectifiers are summarised in Table 1.

One can see that all energy characteristics are proportional to the square of V_{TE}. Clearly, a larger V_{TE} leads to a higher saturated voltage, but more importantly a higher energy per cycle. This is consistent with the figures of merit of TENGs which are typically proportional to the square of the surface charge density of the triboelectric layer [29,30]. In this paper, the focus is on the influences of η and ζ, while assuming constant V_{TE} and C_{T_min}.

2.6.2. Comparison of half-wave and full-wave charge-pumps

From the above table, it can be seen that HW rectifiers are more efficient than FW rectifiers: they allow a higher maximum energy ΔE_{max} at the optimum voltage, by a factor of $(\eta + 1)/2$. This maximum energy requires the HW rectifier to have a higher output voltage V_{opt} by a factor of $\eta + 1$, and which places a higher requirement on the interface electronics, which must support and handle a significantly higher voltage.

However, there is one situation in which the FW rectifier provides a higher energy per cycle than a HW rectifier: at the beginning of the pumping process, when V_{rect} is small comparing to V_{TE}. Comparing the values ΔE_0 for the two networks, it can be noted that the energy per cycle is 4 times greater for the FW than for HW networks. This may explain why the FW diode bridge is still largely used for rectifying the TENG output: FW provides better performances when working at voltages much below the optimum one, which is often the case when working with a 1-stage power management circuit and/or when the charging time is a critical issue.

The FW rectifier saturates at a lower voltage than the HW rectifier by a factor of $\eta + 1$, which is always greater than 2 (since $\eta > 1$). Moreover, for a high η the saturation voltage of the FW rectifier is practically independent of η and is close to V_{TE}, whereas for the HW the saturation voltage is ηV_{TE}. However, the FW rectifier reaches saturation at a shorter time, by a factor $2(\eta+1)$, which is at least 4.

2.6.3. Simulations from the obtained formulas

The evolution formulas of the two charge-pumps have been applied to simulate their behaviour. Simulations of the voltages across C_{rect} with different capacitance variations and with different values of C_{rect} are shown in Fig. 5a and Fig. 5b. As expected, a higher saturated voltage is obtained with increasing capacitance ratio for HW rectifiers (the parameter η), while for FW it gradually tends towards V_{TE} when increasing η. In both cases, the saturated voltages are not related to the value of the storage capacitance (the parameter ζ), as predicted by the analysis (Fig. 6b). Therefore, higher maximum energy per cycle is achieved with higher capacitance variation, as shown in Fig. 5c and d. Fig. 6c, and the maximum energy per cycle is independent from the storage capacitance value (the parameter ζ). Consequently, increasing the capacitance variation is a keyway to improve the performances for both FW and HW rectifiers, and this remains true regardless the conditioning circuit for any electrostatic transducer [2].

As shown in the simulations, in agreement with (15), the energy per cycle is initially increasing with time going on to approach a maximum value, and then it drops to zero due to saturation of the output voltage (see Fig. 6a and b). As with the saturated voltage, there is a larger energy per cycle at the i^{th} cycle (ΔE_i^{FW} or ΔE_i^{HW}) and also a larger maximum energy per cycle (ΔE_{max}^{FW} or ΔE_{max}^{HW}) with a larger capacitance change. Generally, $\Delta E_i^{HW} > \Delta E_i^{FW}$, except for the early cycles corresponding to very low TENG bias voltages. The storage capacitance has little impact on the maximum energy per cycle but its value has a strong influence on the time needed to reach the optimal voltage corresponding to the maximum energy. It is important to consider this property when designing power management circuit, the goal of which usually to quickly charge a large storage capacitor. This motivates the use of a two-stage power management architecture.

3. Analysis of the 2-stage power management circuit

Like any charge pump ending in a saturation, the FW and HW rectifiers have an optimal regime corresponding to a maximum converted energy per cycle. This regime is determined by the value of the saturation output voltage V_{sat}: the energy converted per cycle is close to ΔE_{max} if the voltage across C_{rect} is close to V_{opt} (which, for the two circuits considered here, is equal to $V_{sat}/2$). However, if a charge pump reaches saturation, then the energy converted per cycle drops to zero. To avoid this, an additional circuit is needed that remove the energy from the capacitor C_{rect} so to maintain its voltage at the optimal level V_{opt}. The rate of this energy removal is equal to the maximal converted power ΔE_{max}/T, and the average value of the current is equal to $\Delta E_{max}/(V_{opt}T)$, where T is the period of the mechanical cycle. This operation cannot be achieved by connecting the load to C_{rect}: indeed, V_{opt} is at least of the same order as the built-in voltage of the TENG V_{TE} (tens or hundreds of volts), and it is therefore hardly compatible with a useful load requiring supply voltage typically of a few volts. This second power conversion stage plays two roles: (i) a DC-DC conversion from V_{opt} to V_{store} to generate a low voltage for the load, (ii) a transfer of the energy accumulated by the charge pump from C_{rect} to C_{store} (and to the load) with

Table 1
Formulas for FW and HW rectifiers.

	Generic formulas	Full wave rectifier ($\epsilon \ll 1$)	Half wave rectifier ($\epsilon \ll 1$)
β	–	$V_{TE}\frac{2(\eta-1)}{\zeta}$	$V_{TE}\frac{\eta-1}{\zeta}$
ϵ	$1-\alpha$ ($\alpha < 1$)	$\frac{2(\eta+1)}{\zeta}$	$\frac{1}{\zeta}$
V_{sat}	$\frac{\beta}{\epsilon}$	$V_{TE}\frac{\eta-1}{\eta+1}$	$V_{TE}(\eta-1)$
V_{opt}	$\frac{\left(\frac{1}{\epsilon}-1\right)\beta}{2-\epsilon}$	$\frac{1}{2}V_{TE}\frac{\eta-1}{\eta+1}$	$\frac{1}{2}V_{TE}(\eta-1)$
ΔE_{max}	$\frac{C_{rect}}{2}\frac{\beta^2}{\epsilon(2-\epsilon)}$	$\frac{C_{T\_min}{V_{TE}}^2}{2}\bullet\frac{(\eta-1)^2}{\eta+1}$	$\frac{C_{T\_min}{V_{TE}}^2}{2}\bullet\frac{(\eta-1)^2}{2}$
ΔE_0	$\frac{C_{rect}}{2}\beta^2$	$\frac{C_{T\_min}{V_{TE}}^2}{2}\bullet 4\frac{(\eta-1)^2}{\zeta}$	$\frac{C_{T\_min}{V_{TE}}^2}{2}\bullet\frac{(\eta-1)^2}{\zeta}$
i_{sat}	$\frac{3}{\epsilon}$	$\frac{3\zeta}{2(\eta+1)}$	3ζ
$\Delta E_{avg\ i}$	$\frac{1}{i}\frac{C_{rect}}{2i}\left(\frac{\beta}{\epsilon}\right)^2(1-\exp(-i\epsilon))^2$	$\frac{C_{rect}{V_{TE}}^2}{2i}\left(\frac{\eta-1}{\eta+1}\right)^2\left\{1-exp\left[-\frac{2}{\zeta}\frac{(\eta+1)i}{}\right]\right\}^2$	$\frac{C_{rect}{V_{TE}}^2}{2i}(\eta-1)^2\left\{1-exp\left[-\frac{2}{\zeta}\frac{(\eta+1)i}{}\right]\right\}^2$

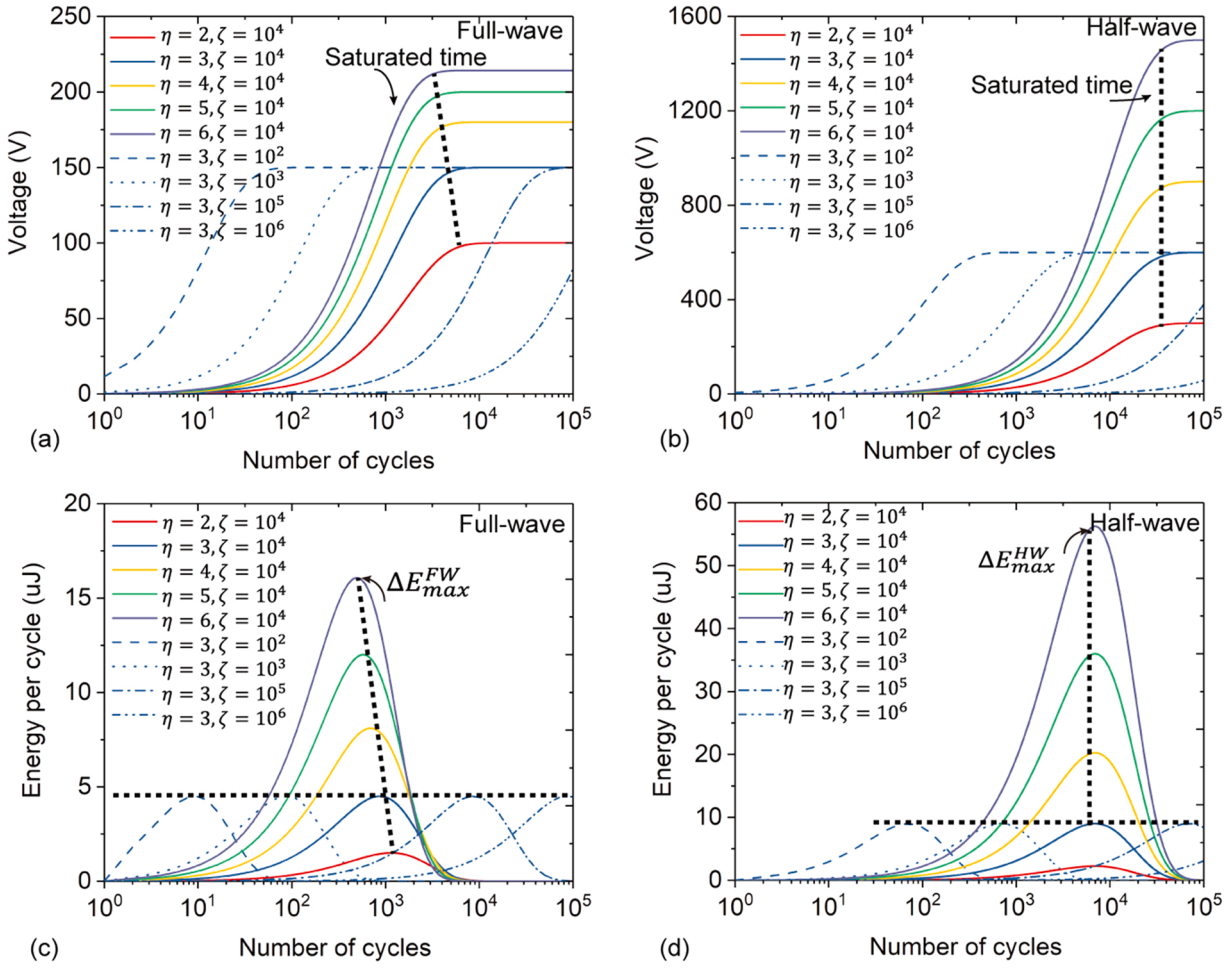

Fig. 5. Simulated voltage across C_{rect} versus number of mechanical cycles with different capacitance variations and storage capacitances, and corresponding energy per cycles. Voltage with (a) full-wave rectifiers and (b) half-wave rectifiers. Energy per cycle with full-wave rectifiers (c) and half-wave rectifiers (d). C_{T_min} = 100 pF and V_{TE} = 300V.

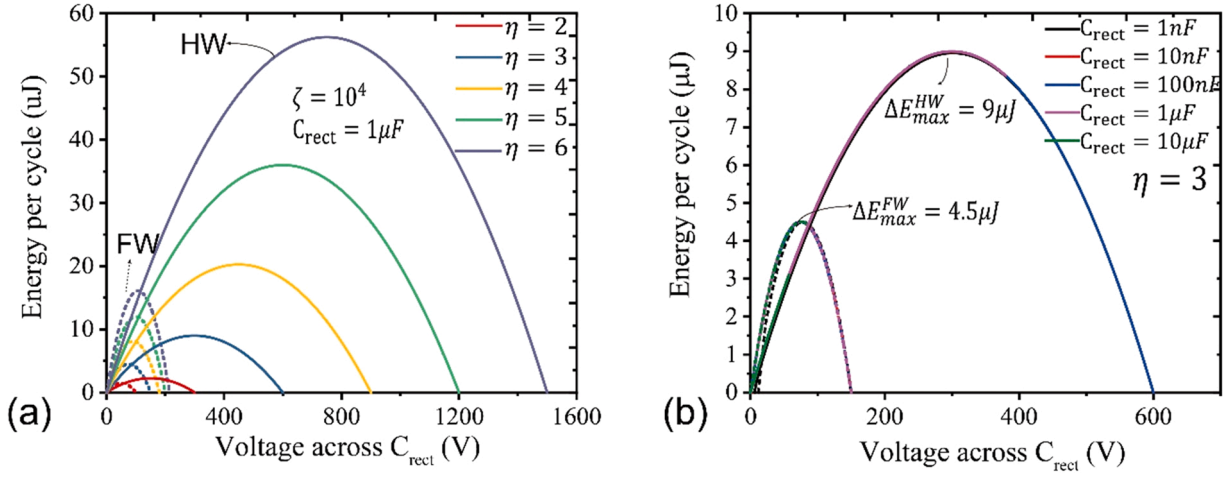

Fig. 6. Simulated energy per cycle versus voltage across C_{rect} for full-wave and half-wave rectifiers. With different TENG's capacitance variations (a) and storage capacitance (b). C_{T_min} = 100 pF and V_{TE} = 300 V.

the optimum transfer power $\Delta E_{max}/T$, keeping the voltage across C_{rect} close to V_{opt}.

In the following, the previous theory has been applied on HW and FW rectifiers to the analysis of the 2-stage PMC (2SPMC) (Fig. 7a). In the st stage, the output capacitor of the rectifier C_{rect} acts as a high-voltage buffer, and the second stage consists here in a buck DC-DC down converter. It consists of a controlled switch, an inductor, and a freewheel diode. The output capacitor C_{store} is large ($C_{store} >> C_{rect}$) and held at V_{store} by the 2-stage PMC. For the switch control, there are two main options: (i) a full-hysteresis switch (FHSW) that is turned ON at some

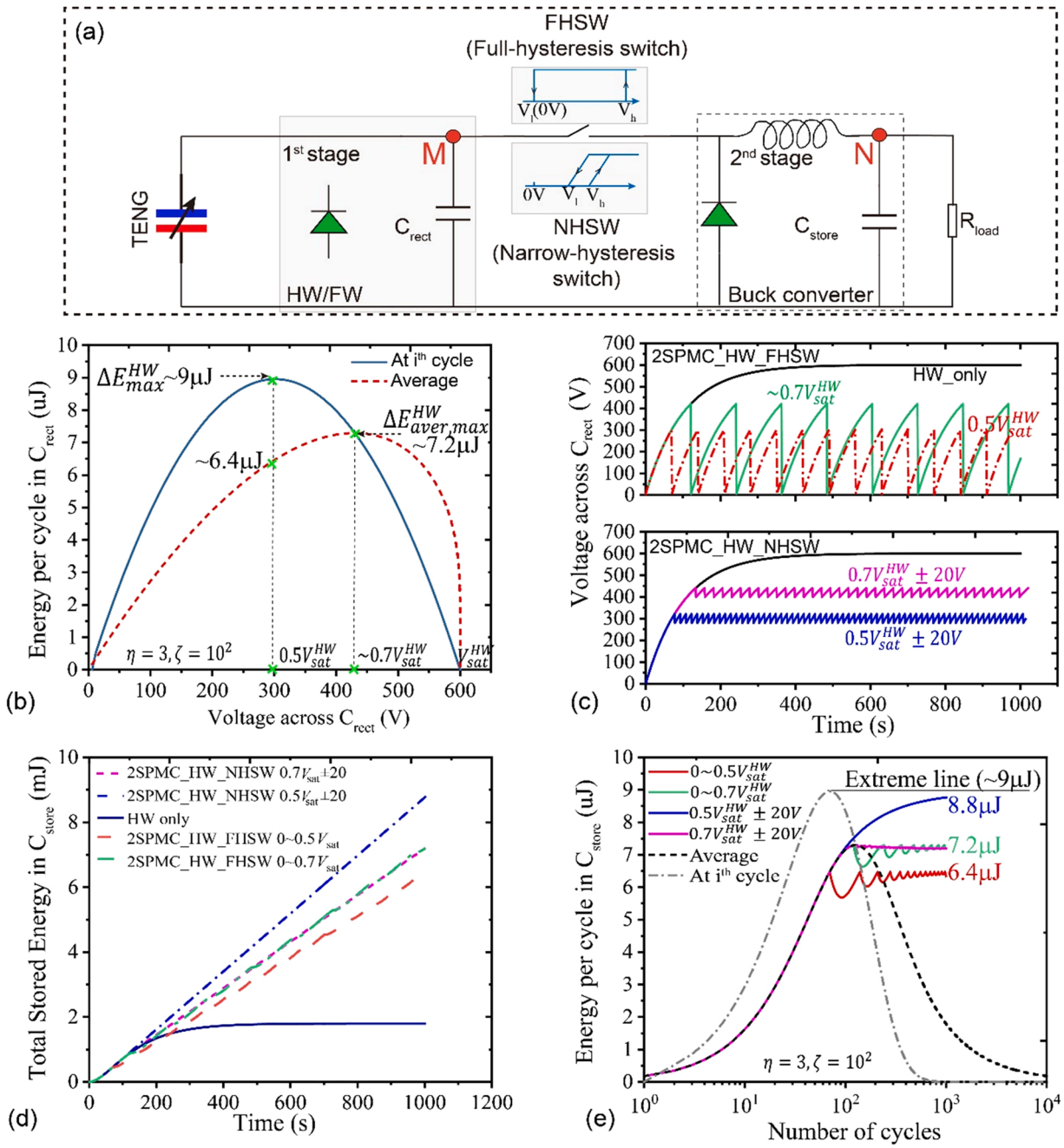

Fig. 7. Simulation results of the two-stage power management circuit (2SPMC). (a) Schematic of the 2SPMC. (b) Energy and average energy per cycle in C_{rect} using the HW rectifier. (c) Voltage across C_{rect} with $V_{opt}^{HW} = 0.5V_{sat}^{HW}$ (red-dashed line) or $V_{opt}^{HW} = 0.7V_{sat}^{HW}$ (green line), for 2SPMC with a HW rectifier and full-hysteresis switch (2SPMC_HW_FHSW), or a narrow-hysteresis switch (2SPMC_HW_NHSW). (d) Comparison of total stored energy curves using different configurations. (e) Energy per cycle in C_{store}, average energy per cycle and at the ith cycle using HW without the switch (black and grey curves, same data as that in b), using HW rectifier and 2SPMC with different optimized voltage setups and switches (colored lines).

high voltage of $V_{\rm rect}$, and is turned OFF when $V_{\rm rect}$ reaches 0 V; (ii) a narrow-hysteresis switch (NHSW) that is turned ON when $V_{\rm rect}$ is slightly above $V_{\rm opt}$ and turned OFF when $V_{\rm rect}$ is slightly below $V_{\rm opt}$. The FHSW is easier to obtain and to control, but the NHSW leads to greater converted power as it will be demonstrated in the following.

3.1. Impact of the switch hysteresis

3.1.1. The full hysteresis

At each actuation of the switch, in the case of the full hysteresis, the output capacitor $C_{\rm store}$ receives the energy

$$E_{C_{\rm rect}}^{\rm FHSW} = \frac{1}{2}\gamma C_{\rm rect} \quad V_{\rm h}^2 \tag{47}$$

where $V_{\rm h}$ is the voltage across $C_{\rm rect}$ at which the switch is turned ON, and γ is the energy transfer efficiency of the DC-DC converter based on a practical hardware implementation. If the energy transfer from $C_{\rm rect}$ to $C_{\rm store}$ takes a negligible time compared to the charging time of $C_{\rm rect}$, the average power received by $C_{\rm store}$ can be calculated as

$$P_{\rm av}^{\rm FHSW} = \frac{E_{C_{\rm rect}}^{\rm FHSW}}{iV_{\rm h}T} \tag{48}$$

where i^{V_h} is the number of cycles required by V_{rect} to reach V_h from zero, and T is the period of one pumping cycle at the first stage. This number can be calculated with (21) by letting $V_0 = 0$:

$$i^{V_h} = -\frac{1}{\epsilon_{rect-2st}} \ln\left(1 - \frac{\epsilon_{rect-2st}}{\beta_{rect-2st}} V_h\right) \tag{49}$$

where $\epsilon_{rect-2st}$ and $\beta_{rect-2st}$ correspond to ϵ and β for the rectifier in the 2-stage PMC respectively. We obtained

$$P_{av}^{FHSW} = \frac{\frac{1}{2}\gamma C_{rect} \quad V_h^2}{-\frac{1}{\epsilon}\ln\left(1 - \frac{\epsilon_{rect-2st}}{\beta_{rect-2st}} V_h\right) T} \tag{50}$$

It can be seen that there is an optimal V_h maximizing P_{av}^{FHSW}. However, it cannot be expressed analytically from Eq. (50). The simulation in Fig. 7b shows that for the HW charge pumps used in the first stage, the optimal value of V_h is $0.7V_{sat}^{HW}$. An identical result would be obtained with the FW rectifier ($V_h = 0.7V_{sat}^{FW}$).

3.1.2. The narrow hysteresis

The performance of the narrow hysteresis switch configuration can be evaluated in a similar manner. The energy transferred at each switch actuation cycle of is given by

$$E_{C_{rect}}^{FHSW} = \frac{1}{2}\gamma C_{rect} \quad (V_h^2 - V_l^2) \tag{51}$$

where V_l is the low activation voltage of the switch. Assuming that V_l and V_h are close to V_{opt}, the energy generated on V_{rect} by the first stage at each pumping cycle can be considered almost constant and equal to ΔE_{max}. If the increase from V_l to V_h lasts k cycles of the TENG capacitance variation, the energy transferred is given by $E_{C_{rect}}^{FHSW} \approx \gamma k \Delta E_{max}$. The average power generated on C_{store} can be calculated as follows:

$$P_{av}^{NHSW} = \frac{\gamma k \Delta E_{max}}{kT} = \frac{\gamma \Delta E_{max}}{T} \tag{52}$$

Ideally, V_h and V_l should be as close to V_{opt} as possible, which means that the ideal configuration is for k equal to 1. However, this will maximize the number of switch actuations, which consumes some power, especially if electrical control is needed to synchronize with the charge pump. For this reason, it is best if the hysteresis loop is not too narrow. The optimal value of k is related to the energy cost of activating the Buck switch, and it must be optimised for each particular hardware implementation.

3.1.3. Simulation results

In Fig. 7b, it can be observed that the energy per cycle for the HW PMC at the i^{th} cycle ΔE_i^{HW} reaches its maximum value for $V_{rect}^{HW} = 0.5V_{sat}^{HW}$, which is consistent with the formulas in Table 1. A similar result is obtained with the FW rectifier. However as mentioned earlier, the average energy per cycle $\Delta E_{avg\ i}$ reaches its maximum for a voltage on C_{rect} of $0.7V_{sat}$. This means that for the FW and HW rectifiers in a 2-stage PMC, the highest charging efficiency with a full-hysteresis switch is obtained if the switch is ON at $0.7V_{sat}$, whereas with a narrow-hysteresis switch, the switch should be ON/OFF around $0.5V_{sat}$, at least if the power required to operate the switch is negligible.

Fig. 7c-e compare simulations of the 2-stage configuration with both FHSW and NHSW strategies. Fig. 7c shows the voltages across C_{rect} when using a 2-stage PMC with different switch actuation voltages and full- or narrow- hysteresis switches. Fig. 7d shows the corresponding total energy in C_{store}. With only the HW diode bridge as PMC, the output voltage and so the collected energy saturate, and then energy per cycle (i.e. the power) reaches zero after some time (Fig. 7e). On the other hand, the total harvested energy using the FHSW or NHSW strategies increases continuously since C_{rect} has never been charged to saturation due to the switch that regularly releases the harvested energy stored in C_{rect}. Thus, the inherent drawback of the voltage saturation in stable charge-pumps such as FW and HW rectifiers is overcome.

Furthermore, by comparing in Fig. 7e the total energy harvested using the 2-stage methods with different switch controls, as expected, the best performance is obtained with $V_{opt} = 0.5V_{sat}^{HW}$ (solid blue plot), which yields an average energy per cycle in steady-state operation that reaches the maximum theoretical value of the HW (~8.8 μJ/cycle). The green line shows the evolution of the energy per cycle for a 2-stage PMC with a HW rectifier and a full-hysteresis (FH) switch with setting $V_{opt} = 0.7V_{sat}^{HW}$, which is supposed to be the optimal voltage of the FH operation. The steady-state energy per cycle is 7.2 μJ. For sake of comparison, the red line shows the evolution for the same configuration but for V_h=$0.5V_{sat}^{HW}$: the steady state energy per cycle is now 6.4 μJ, which is less than the case for V_h=$0.7V_{sat}^{HW}$. These results are in good agreement with the theory: (i) they confirm the superiority of the energy conversion of the configuration of the narrow hysteresis, (ii) they confirm the optimal value of thresholds for the configuration of full and narrow hysteresis.

3.2. Charging time of a large capacitor

Most systems are supplied with only a few volts delivered by a battery or large capacitor to limit the voltage variation. However, if a large (and discharged) capacitor is connected at the output of a FW or HW rectifier in a typical single stage configuration, at low voltages the incoming power (the energy per cycle ΔE_0) is very low and the charging process can take a long time. As explained above, the problem can be solved by using a power management circuit with a 2-stage PMC where the buffer capacitor C_{rect} can be kept relatively small. In this section we estimate the gain in the charging time provided by a 2-stage PMC compared to a 1-stage one when charging C_{store} to a certain voltage V_{store}. Two configurations have been considered: the 1-stage PMC with C_{store} connected at the output, and a 2-stage configuration with C_{store} connected at the output of the 2nd stage while C_{rect} is connected at the output of the 1st stage. In what follows, $C_{store} > > C_{rect} > > C_{min}$, $C_{max} > > C_{min}$ and $V_{TE} > > V_{store}$. These assumptions correspond to most practical cases and will allow us to simplify the formulas.

Considering that V_{store} is much smaller than V_{TE}, with a 1-stage PMC, the energy at each cycle can be considered as constant and equal to ΔE_0 (see Eq. (19)). Therefore, the charging time (i.e. the number of cycles) to charge C_{store} is given by:

$$i_{C_{st-1st}} \approx \frac{E_{store}}{\Delta E_0} = \frac{\frac{C_{store}}{2} V_{store}^2}{\frac{C_{store}}{2} \beta_{store-1st}^{\ 2}} = \frac{V_{store}^2}{\beta_{store-1st}^{\ 2}} \tag{53}$$

Here C_{rect} in the previous equations has been renamed to C_{store} and β to $\beta_{store-1st}$.

With the 2-stage configuration, the charging time can be estimated as the sum of the times required for the 1st stage to charge C_{rect} to V_{opt}, and then to charge C_{store} to V_{store} by transferring ΔE_{max} at each cycle. First $i_{C_{rect-2st}}$, the charging time of C_{rect}, is calculated with (21) by setting V_0= 0 and V_i=V_{opt} taken from (18). It leads to:

$$i_{C_{rect-2st}} = \frac{1}{\epsilon_{rect-2st}} \ln 2 \tag{54}$$

where $\epsilon_{rect-2st}$ corresponds to ϵ for the rectifier in the 2-stage PMC. $i_{C_{store-2st}}$, the charging time of C_{store} in the 2nd stage, can be calculated by assuming that the energy transfer rate is constant and equal to ΔE_{max} (from (18)) per cycle (dissipative effects in the transfer have been neglected, i.e. $\gamma = 1$):

$$i_{C_{store-2st}} = \frac{E_{store}}{\Delta E_{max}} = \frac{\frac{C_{store}}{2} V_{store}^2}{\frac{C_{rect}}{2} \frac{\beta_{rec-2st}^{\ 2}}{2\epsilon_{rect-2st}}} = \frac{C_{store}}{C_{rect}} \frac{2\epsilon_{rect-2st} V_{store}^2}{\beta_{rec-2st}^{\ 2}} \tag{55}$$

The charging time is then calculated as follows:

$$G_{\text{ch.time}} = \frac{i_{C_{\text{store}-1\text{st}}}}{i_{C_{\text{rect}-2\text{st}}} + i_{C_{\text{store}-2\text{st}}}} = \frac{\frac{V_{\text{store}}^2}{\beta_{\text{store}-1\text{st}}^2}}{\frac{1}{\epsilon_{\text{rect}-2\text{st}}}\ln 2 + \frac{C_{\text{store}}}{c_{\text{rect}}}\frac{2\epsilon_{\text{rect}-2\text{st}}V_{\text{store}}^2}{\beta_{\text{rec}-2\text{st}}^2}} \quad (56)$$

If $C_{\text{store}} >> C_{\text{rect}}$, $i_{C\text{rect-2st}}$ is negligible compared to $i_{C\text{store-2st}}$, the charging time gain can be simplified to

$$G_{\text{ch.time}} \approx \frac{1}{2\epsilon_{\text{rect}-2\text{st}}}\frac{C_{\text{rect}}}{C_{\text{store}}}\frac{\beta_{\text{rec}-2\text{st}}^2}{\beta_{\text{store}-1\text{st}}^2} \quad (57)$$

Since for both HW and FW rectifiers we have $\frac{\beta_{\text{rec}-2\text{st}}^2}{\beta_{\text{store}-1\text{st}}^2} = \left(\frac{\zeta_{\text{store}-1\text{st}}}{\zeta_{\text{rect}-2\text{st}}}\right)^2 = \left(\frac{C_{\text{store}}}{C_{\text{rect}}}\right)^2$, we obtained

$$G_{\text{ch.time}} \approx \frac{C_{\text{store}}}{2\epsilon_{\text{rect}-2\text{st}}C_{\text{rect}}} \quad (58)$$

Replacing $\epsilon_{\text{rect}-2\text{st}}$ with its expressions from Table 1, we obtain for the FW rectifier $G_{\text{ch.time}}^{\text{FW}} \approx \frac{C_{\text{store}}}{4C_{\text{T\_max}}}$ and for the HW rectifier $G_{\text{ch.time}}^{\text{HW}} \approx \frac{C_{\text{store}}}{2C_{\text{T\_min}}} = 2\eta G_{\text{ch.time}}^{\text{FW}}$. It can be observed that the gain provided by a 2-stage configuration using a HW rectifier is at least twice that obtained using a FW rectifier and increases proportionally with η.

4. Experimental results

Experiments were performed with a contact-separate mode TENG based on a macro-shaped conductive polyurethane foam (C-PUF) [31]. One advantage of this device is that its capacitance variation can easily be adjusted by varying the contact force. The setup is shown in Fig. 9. The TENG excited with a vibration shaker (MODAL SHOP K2007E01), controlled by a signal generator (Tektronix AFG3102) with a frequency of 5 Hz. The capacitance variation was measured using the method described in [22], showing variations from $\eta = 1.39$ to $\eta = 3.37$ with contact forces from 2 N to 10 N. The output voltage of the capacitors was monitored with high-impedance followers (OPA 445), and capacitor dividers were used to adapt the signal to the voltage limitation of the amplifier. The inductor value of the DC-DC buck converter is 100 mH. Two low-loss diodes were in series to increase the inverse breakdown voltage up to 600 V.

4.1. Performances of the FW and HW rectifiers in the 1-stage conditioning-circuit

First, experiments using single FW and HW rectifiers to charge C_{rect} were performed (circuits in Fig. 3a and Fig. 4a), whose goal is to demonstrate the optimal regimes of the FW/HW rectifiers. The time

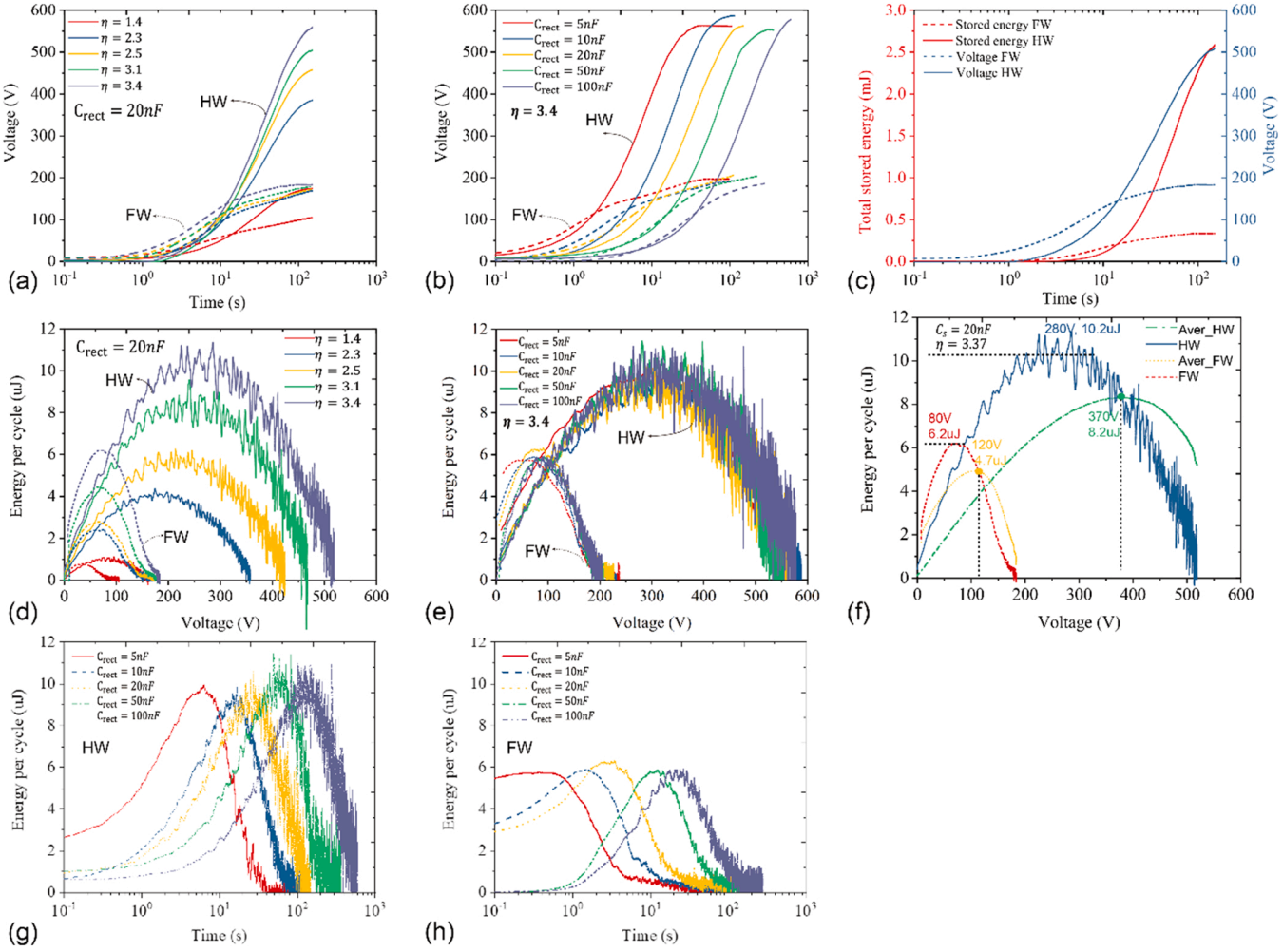

Fig. 8. Electrical performances of the TENG charging a capacitor with FW or HW rectifiers in a one-stage conditioning circuit. Voltage across the storage capacitor versus time with different TENG's capacitance variations (a) and output capacitances C_{rect} (b) charged with full-wave (dash line) and half-wave (solid line) diode bridges. (c) Voltage and total stored energy versus time when capacitance variation is 3.37. Energy per cycle in C_{rect} versus voltage across C_{rect} with different TENG's capacitance variations (d) and and output capacitances C_{rect} (e). Comparisons of the energy per cycle and average energy per cycle for FW and HW rectifiers (f). Energy per cycles for HW (g) and FW (h) rectifiers versus the operation time.

evolution of the voltage across C_{rect} with different TENG's max-to-min capacitance ratios (η) and C_{rect} values are shown in Fig. 8a,b. With a capacitance variation of $\eta = 3.4$, the saturated voltage of HW is $V_{sat}^{HW} \approx 580$V, while that of the FW is $V_{sat}^{FW} \approx 190$V, resulting in the maximal total stored energy of the HW ~ 9 times higher than that of FW (Fig. 8c). The maximum energy per cycle is ~10 μJ/cycle (HW) and ~6 μJ/cycle (FW) (Fig. 8e). When η decreases from $\eta = 3.4$ to $\eta = 1.4$, the saturated voltage drops to ~174 V and ~104 V for HW and FW, respectively (Fig. 8a).

The voltage across C_{rect} using the HW rectifier firstly increases with a lower slope than with the FW, and then increases faster after a few operation cycles, confirming again that FW has better performances only at the beginning of the charging [20]. This can also be seen in the energy-per-cycle graphs shown in Fig. 8d-f.

The maximum energy per cycle is independent of the value of C_{rect} (Fig. 8e), and a larger C_{rect} leads to a longer time to approach the maximum energy per cycle (Fig. 8g,h). Then, for a given number of operation cycles, a smaller C_{rect} and a higher capacitance variation result in a higher maximum energy per cycle. As in the theoretical analysis, the energy per cycle versus output voltage reaches a maximum value at $0.5V_{sat}^{HW}$. Likewise, the maximum average energy per cycle (calculated from a fully discharged C_{rect}) is appearing at a higher maximum output voltage, around $0.7V_{sat}^{HW}$ (Fig. 4f).

In this experiment, the output voltage for the maximum energy per cycle is 80 V with the FW rectifier, corresponding to an energy per cycle of 6.2 μJ/cycle, while the maximum average energy per cycle is at 120 V for an energy per cycle of 4.7 μJ/cycle. With the HW rectifiers, the maximum energy per cycle is at a voltage ~280 V, corresponding to an energy per cycle of 10.2 μJ/cycle, while the maximum average energy per cycle is at the voltage of 370 V for an average energy per cycle of 8.2 μJ/cycle.

4.2. Performances using the two-stage power management circuits

In the following, the performances of two-stage management circuits are compared with the 1-stage configuration. The two-stage configuration is implemented with a Buck DC-DC down converter having an electrostatic plasma switch made of a flexible copper wire of 120 μ μm in diameter and a fixed plate in aluminium. The ON and OFF actuation voltage can be adjusted by varying the stiffness of the copper wire and its distance with the 2nd electrode thanks to a 3-axis displacement platform [32]. The switch was connected on one side to the buffer capacitor (C_{rect}) and on the other side to the output capacitor C_{store}. The setup of the 2-stage PMC is shown in Fig. 9.

The electrical performances of five conditioning-circuit configurations to charge C_{store} have been compared, i.e., (i) FW_only; (ii) HW_only; (iii) 2-stage PMC with a FW rectifier and full-hysteresis switch (2SPMC_FW_FHSW) setting ON voltage at $0.7V_{sat}^{FW} \sim 140V$; (iv) 2SPMC with a HW rectifier and full-hysteresis switch (2SPMC_HW_FHSW) setting ON voltage at $0.7V_{sat}^{HW} \sim 360V$; and (v) 2-stage PMC with a HW rectifier and narrow-hysteresis switch (2SPMC_HW_NHSW) setting ON voltage at ON voltage at $0.5V_{sat}^{HW} \sim 280V$. the buffer capacitor $C_{rect} \approx 5$ nF, the reservoir capacitor $C_{store} = 22$ μF and the Buck inductor is of 100 mH.

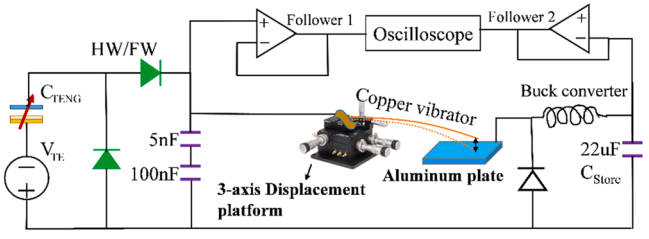

Fig. 9. The schematic of the automatic hysteresis electrostatic switch and the electrical setup.

The charging curves of C_{rect} and C_{store} under the configurations (iii), (iv) and (v) are shown in Fig. 10a, b and c, respectively. The voltage across C_{store} increases step by step synchronously with the switch actuation. The narrow-hysteresis is obtained at the cost of a higher frequency switch actuation compared to the full-hysteresis switch. The charging curves of C_{store} for the five configurations are summarized in Fig. 10d, which shows that the 2-stage HW rectifier with the narrow hysteresis results in the fastest charging speed, while only the HW is the slowest.

After reaching a maximum of 9.8 μJ with only the HW rectifier, as predicted by the simulations, the energy per cycle quickly decreases towards zero because of the charge pump saturation. In steady-state, the maximum average energy per cycle in C_{rect} is obtained with the narrow hysteresis and the HW, but is only 7.0 μJ/cycle (Fig. 10e). The difference is attributed to the inherent energy dissipation of the switch and capacitors. The maximum average energy per cycle in C_{store} is 3.9 μJ/cycle, 56% of that of C_{rect}, because of the further dissipations of the switch, capacitors and inductors. This corresponds to a total energy transferring efficiency of 40% (3.9/9.8). With the FW and the narrow hysteresis switch, the total energy transferring efficiency is of 20% (2/9.8). With a 1-stage PMC, the efficiency tends to be zero at the steady state because of the output voltage saturation.

To quantitatively compare the charging efficiency of different conditioning circuits, we normalized the charging time for different circuit configurations by setting the time of FW only to charge C_{store} to 8 V as 100%, which is shown in Fig. 10f. It can be concluded that 85.5% of the charging time is saved using the 2-stage PMC with the HW rectifier compared to 1-stage PMC with a FW rectifier. Further improvement can be achieved if the switch can be optimized for a better control of the hysteresis and a reduction of its current leakage and energy consumption [11].

5. Conclusions

This paper has presented a comprehensive analysis for the rectification of the AC signal generated by an electrostatic kinetic energy generator based on stable charge pumps. It led to new generic formulas for various quantities, such as the optimal bias voltage, the maximum energy converted, or the number of actuation cycles required to reach these values. Then, exact formulas for half-wave and full-wave diode bridges were derived, based on the transducer capacitance variations and its internal bias voltage. The voltage dynamics of the energy harvested per cycle when charging a capacitor using a TENG with full-wave and half-wave rectifiers were also analysed and compared. Possible discrepancies between these formulas and the experimental results can be caused by various parasites in the setup, such as reverse current in diodes or input capacitances of measuring instruments.

In addition, how a two stages power management circuit can be used to avoid the output voltage saturation V_{sat} has been investigated. It has been shown that the theoretical optimum ON actuation value V_{opt} of the switch ranges between $0.5V_{sat}$ (when using an ideal narrow hysteresis switch) and $0.7V_{sat}$ (when using a full-hysteresis switch, as it is usually the case in experiments).

Experimental validations were performed using a conductive and macro-shaped polyurethane foam (C-PUF) [31] for the TENG, and a raw plasma switch [32] for the 2-stage PMC implementation. While the HW rectifier provides higher power conversion per cycle at the optimum output voltage, at low output voltage, the FW rectifier wins by a factor of 4 in terms of power generation. By combining a half-wave rectifier and a DC-DC converter controlled by a narrow hysteresis switch, charging time of a 22 μF capacitor to 8 V can be saved by 85.5% compared to a full-wave rectifier. However, the final energy transfer efficiency (40%) can be further improved by improving the efficiency of the automatic switch. One possibility is to use microelectromechanical systems (MEMS) technologies [11] to fabricate and package the switch, so that the turn-on and turn-off voltage can be controlled more precisely.

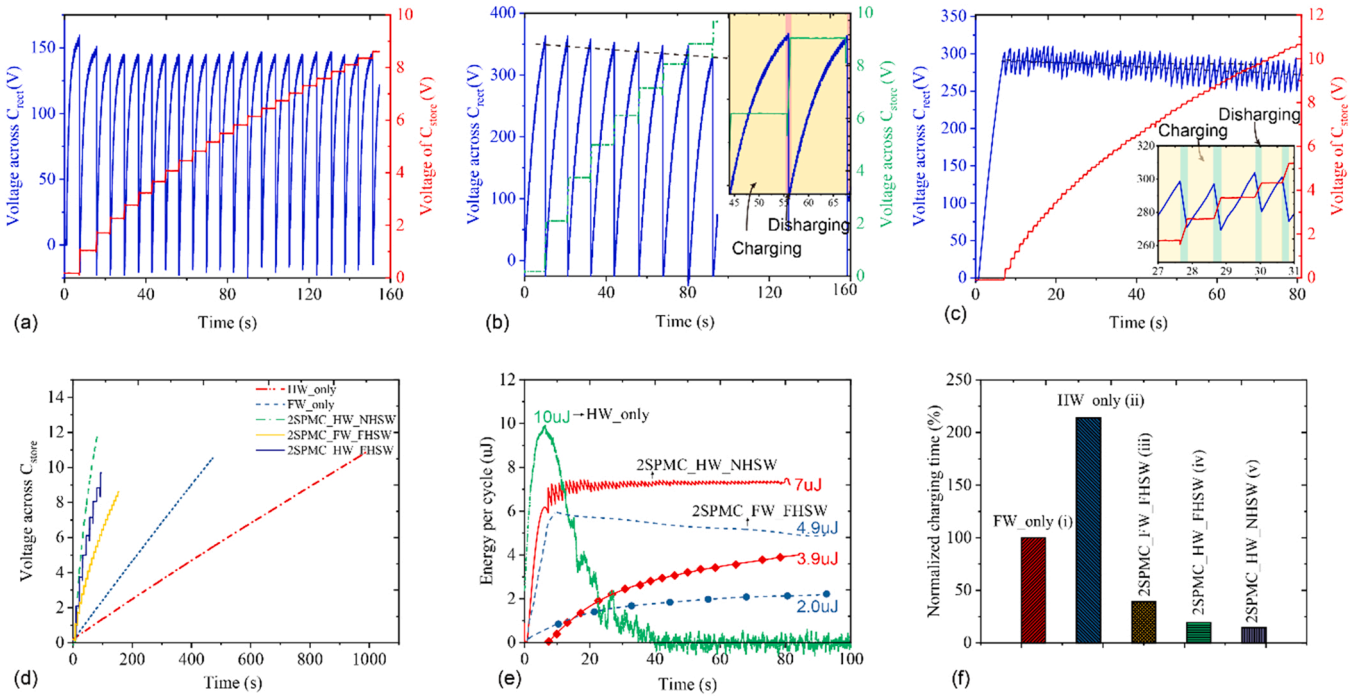

Fig. 10. Electrical performances of the two-stage conditioning circuits with the setup in Fig. 9. (a) Voltages across C_{rect} and C_{store} with a FW rectifier and a full-hysteresis switch (2SPMC_FW_FHSW), (b) Voltages across C_{rect} and C_{store} with a HW rectifier and a full-hysteresis switch (2SPMC_HW_FHSW). (c) Voltages across C_{rect} and C_{store} with a HW rectifier and a narrow-hysteresis switch (2SPMC_HW_NHSW). (d) Curves of charging a 22 uF capacitor with different conditioning methods. (e) Energy per cycle and average energy per cycle in C_{rect} (red) and C_{store} (navy) with different methods. The red dash line indicates the energy per cycle in C_{rect}, while the red block line indicates the energy per cycle in C_{store} under the configuration of 2SPMC_HW_NHSW. The blue dotted line indicates the energy per cycle in C_{rect}, while the blue circle line indicates the energy per cycle in C_{store} under the configuration of 2SPMC_FW_FHSW. (f) Normalized charging time of charging a 22 μF capacitor to 8 V using different methods.

CRediT authorship contribution statement

Hemin Zhang: Conceptualization, Investigation, Validation, Writing - original draft, Visualization, **Dimitri Galayko:** Methodology, Writing - review & editing, **Philippe Basset:** Supervision, Writing - review & editing, Project administration, Funding acquisition.

Declaration of Competing Interest

The authors declare that they have no known competing financial interests or personal relationships that could have appeared to influence the work reported in this paper.

Data availability

Data will be made available on request.

References

[1] F.R. Fan, Z.Q. Tian, Z.L. Wang, Flexible triboelectric generator, Nano Energy 1 (2) (2012) 328–334, https://doi.org/10.1016/j.nanoen.2012.01.004.

[2] P. Basset, E. Blokhina, D. Galayko, Electrostatic Kinetic Energy Harvesting, John Wiley & Sons, 2016, https://doi.org/10.1002/9781119007487.

[3] R. Hinchet, A. Ghaffarinejad, Y. Lu, J.Y. Hasani, S.W. Kim, P. Basset, Understanding and modeling of triboelectric-electret nanogenerator, Nano Energy (2018), https://doi.org/10.1016/j.nanoen.2018.02.030.

[4] M.A. Ben Ouanes, H. Samaali, D. Galayko, P. Basset, et F. Najar, A new type of triboelectric nanogenerator with self-actuated series-to-parallel electrical interface based on self-synchronized mechanical switches for exponential charge accumulation in a capacitor (août), Nano Energy vol. 62 (2019) 465–474, https://doi.org/10.1016/j.nanoen.2019.05.049.

[5] T. Wang, G. Gu, W. Shang, J. Gan, W. Zhang, H. Luo, B. Zhang, P. Cui, J. Guo, F. Yang, G. Cheng, Z. Du, A self-powered photodetector using a pulsed triboelectric nanogenerator for actual working environments with random mechanical stimuli (déc.), Nano Energy vol. 90 (2021), 106518, https://doi.org/10.1016/j.nanoen.2021.106518.

[6] A. Brenes, A. Morel, J. Juillard, E. Lefeuvre, et A. Badel, Maximum power point of piezoelectric energy harvesters: a review of optimality condition for electrical tuning (mars), Smart Mater. Struct. vol. 29 (n° 3) (2020), 033001, https://doi.org/10.1088/1361-665X/ab6484.

[7] F. Xi, Y. Pang, W. Li, T. Jiang, L. Zhang, T. Guo, G. Liu, C. Zhang, Z.L. Wang, Universal power management strategy for triboelectric nanogenerator, Nano Energy 37 (2017) 168–176, https://doi.org/10.1016/j.nanoen.2017.05.027.

[8] X. Cheng, L. Miao, Y. Song, Z. Su, H. Chen, X. Chen, J. Zhang, H. Zhang, High efficiency power management and charge boosting strategy for a triboelectric nanogenerator, Nano Energy 38 (2017) 438–446, https://doi.org/10.1016/j.nanoen.2017.05.063.

[9] W. Shang, et al., Rotational pulsed triboelectric nanogenerators integrated with synchronously triggered mechanical switches for high efficiency self-powered systems (avr), Nano Energy vol. 82 (2021), 105725, https://doi.org/10.1016/j.nanoen.2020.105725.

[10] S. Niu, X. Wang, F. Yi, Y.S. Zhou, Z.L. Wang, A universal self-charging system driven by random biomechanical energy for sustainable operation of mobile electronics, Nat. Commun. (2015) 6, https://doi.org/10.1038/ncomms9975.

[11] H. Zhang, Frédéric Marty, Xin Xia, Yunlong Zi, Tarik Bourouina, Dimitri Galayko, Philippe Basset, Employing a MEMS plasma switch for conditioning high-voltage kinetic energy harvesters, Nat. Commun. vol. 11 (1) (2020) 3221, https://doi.org/10.1038/s41467-020-17019-5.

[12] Y. Zi, J. Wang, S. Wang, S. Li, Z. Wen, H. Guo, Z.L. Wang, Effective energy storage from a triboelectric nanogenerator, Nat. Commun. 7 (2016) 10987, https://doi.org/10.1038/ncomms10987.

[13] Y. Zi, H. Guo, J. Wang, Z. Wen, S. Li, C. Hu, Z.L. Wang, An inductor-free auto-power-management design built-in triboelectric nanogenerators, Nano Energy 31 (2017) 302–310, https://doi.org/10.1016/j.nanoen.2016.11.025.

[14] H. Qin, G. Gu, W. Shang, H. Luo, W. Zhang, P. Cui, B. Zhang, J. Guo, G. Cheng, Z. Du, A universal and passive power management circuit with high efficiency for pulsed triboelectric nanogenerator, Nano Energy 68 (2020), 104372, https://doi.org/10.1016/j.nanoen.2019.104372.

[15] J. Yang, F. Yang, L. Zhao, W. Shang, H. Qin, S. Wang, X. Jiang, G. Cheng, Z. Du, Managing and optimizing the output performances of a triboelectric nanogenerator by a self-powered electrostatic vibrator switch, Nano Energy 46 (2018) 220–228, https://doi.org/10.1016/j.nanoen.2018.02.013.

[16] V. Dorzhiev, A. Karami, P. Basset, F. Marty, V. Dragunov, D. Galayko, Electret-free micromachined silicon electrostatic vibration energy harvester with the Bennet's doubler as conditioning circuit, IEEE Electron Device Lett. 36 (2015) 183–185, https://doi.org/10.1109/LED.2014.2387213.

[17] D. Galayko, A. Dudka, A. Karami, E. O'Riordan, E. Blokhina, O. Feely, P. Basset, Capacitive energy conversion with circuits implementing a rectangular charge-

voltage cycle—part 1: analysis of the electrical domain, IEEE Trans. Circuits Syst. I: Regul. Pap. 62 (11) (2015) 2652–2663, https://doi.org/10.1109/TCSI.2015.2451911.
[18] A. Karami, D. Galayko, P. Basset, Series-parallel charge pump conditioning circuits for electrostatic kinetic energy harvesting, IEEE Trans. Circuits Syst. I: Regul. Pap. Vol. 64 (1) (2017) 227–240. DOI: 10.1109/TCSI.2016.2603064.
[19] A. Ghaffarinejad, J.Y. Hasani, R. Hinchet, Y. Lu, H. Zhang, A. Karami, D. Galayko, S.W. Kim, P. Basset, A conditioning circuit with exponential enhancement of output energy for triboelectric nanogenerator, Nano Energy 51 (2018) 173–184, https://doi.org/10.1016/j.nanoen.2018.06.034.
[20] A. Ghaffarinejad, J.Y. Hasani, D. Galayko, P. Basset, Superior performance of half-wave to full-wave rectifier as a power conditioning circuit for triboelectric nanogenerators: application to contact-separation and sliding mode TENG, Nano Energy 66 (2019), 104137, https://doi.org/10.1016/j.nanoen.2019.104137.
[21] K. Tao, H. Yi, Y. Yang, H. Chang, J. Wu, L. Tang, Z. Yang, N. Wang, L. Hu, Y. Fu, J. Miao, Origami-inspired electret-based triboelectric generator for biomechanical and ocean wave energy harvesting, Nano Energy 67 (2020), 104197, https://doi.org/10.1016/j.nanoen.2019.104197.
[22] Y. Lu, E. O'Riordan, F. Cottone, S. Boisseau, D. Galayko, E. Blokhina, F. Marty, P. Basset, A batch-fabricated electret-biased wideband MEMS vibration energy harvester with frequency-up conversion behavior powering a UHF wireless sensor node, J. Micromech. Microeng. 26 (12) (2016), 124004, https://doi.org/10.1088/0960-1317/26/12/124004.
[23] A. Karami, P. Basset, et D. Galayko, A novel characterization method for accurate lumped parameter modeling of electret electrostatic vibration energy harvesters, 1–1, IEEE Electron Device Lett. (2017), https://doi.org/10.1109/LED.2017.2682232, 1–1.
[24] S. Niu, Y.S. Zhou, S. Wang, Y. Liu, L. Lin, Y. Bando, Z.L. Wang, Simulation method for optimizing the performance of an integrated triboelectric nanogenerator energy harvesting system, Nano Energy vol. 8 (2014) 150–156, https://doi.org/10.1016/j.nanoen.2014.05.018.
[25] S. Niu, et al., Theory of sliding-mode triboelectric nanogenerators, Adv. Mater. vol. 25 (43) (2013) 6184–6193, https://doi.org/10.1002/adma.201302808.
[26] S. Wang, Y. Xie, S. Niu, L. Lin, C. Liu, Y.S. Zhou, Z.L. Wang, Maximum surface charge density for triboelectric nanogenerators achieved by ionized-air injection: methodology and theoretical understanding, Adv. Mater. 26 (39) (2014) 6720–6728, https://doi.org/10.1002/adma.201402491.
[27] W. Liu, Z. Wang, G. Wang, G. Liu, J. Chen, X. Pu, Y. Xi, X. Wang, H. Guo, C. Hu, Z. L. Wang, Integrated charge excitation triboelectric nanogenerator, Nat. Commun. 10 (2019) 1426, https://doi.org/10.1038/s41467-019-09464-8.
[28] S. Niu, Z.L. Wang, Theoretical systems of triboelectric nanogenerators, Nano Energy 14 (2015) 161–192, https://doi.org/10.1016/j.nanoen.2014.11.034.
[29] Y. Zi, S. Niu, J. Wang, Z. Wen, W. Tang, et Z. L. Wang, Standards and figure-of-merits for quantifying the performance of triboelectric nanogenerators (déc), Nat. Commun. vol. 6 (nº 1) (2015) 8376, https://doi.org/10.1038/ncomms9376 (déc).
[30] J. Peng, S.D. Kang, et G. J. Snyder, Optimization principles and the figure of merit for triboelectric generators (déc.), Sci. Adv. vol. 3 (nº 12) (2017) eaap8576, https://doi.org/10.1126/sciadv.aap8576 (déc.).
[31] H. Zhang, Y. Lu, A. Ghaffarinejad, P. Basset, Progressive contact-separate triboelectric nanogenerator based on conductive polyurethane foam regulated with a bennet doubler conditioning circuit, Nano Energy 1 (2018), 51:10-8. DOI: 10.1016/j.nanoen.2018.06.038.
[32] H. Zhang, D. Galayko, P. Basset, A self-sustained energy storage system with an electrostatic automatic switch and a buck converter for triboelectric nanogenerators, J. Phys.: Conf. Ser. vol. 1407 (1) (2019), 012016, https://doi.org/10.1088/1742-6596/1407/1/012016.